PHYSICAL REVIEW B **87**, 205314 (2013)

Ferromagnetism and infrared electrodynamics of $Ga_{1-x}Mn_xAs$

B. C. Chapler,[1] S. Mack,[2,3,*] R. C. Myers,[4] A. Frenzel,[1] B. C. Pursley,[1] K. S. Burch,[5] A. M. Dattelbaum,[6] N. Samarth,[7]
D. D. Awschalom,[2] and D. N. Basov[1]
[1]*Physics Department, University of California-San Diego, La Jolla, California 92093, USA*
[2]*Center for Spintronics and Quantum Computation, University of California-Santa Barbara, California 93106, USA*
[3]*Naval Research Laboratory, Washington, DC 20375, USA*
[4]*Department of Materials Science and Engineering, Ohio State University, Columbus, Ohio 43210, USA*
[5]*Department of Physics and Institute for Optical Sciences, University of Toronto, Toronto, Ontario, Canada, M5S 1A7*
[6]*Los Alamos National Laboratory, Los Alamos, New Mexico 87545, USA*
[7]*Department of Physics, The Pennsylvania State University, University Park, Pennsylvania 16802, USA*

(Received 16 April 2013; published 29 May 2013)

We report on the magnetic and the electronic properties of the prototype dilute magnetic semiconductor $Ga_{1-x}Mn_xAs$ using infrared (IR) spectroscopy. Trends in the ferromagnetic transition temperature T_C with respect to the IR spectral weight are examined using a sum-rule analysis of IR conductivity spectra. We find nonmonotonic behavior of trends in T_C with the spectral weight to effective Mn ratio, which suggest a strong double-exchange component to the FM mechanism, and highlights the important role of impurity states and localization at the Fermi level. Spectroscopic features of the IR conductivity are tracked as they evolve with temperature, doping, annealing, As-antisite compensation, and are found only to be consistent with a Mn-induced IB scenario. Furthermore, our detailed exploration of these spectral features demonstrates that seemingly conflicting trends reported in the literature regarding a broad mid-IR resonance with respect to carrier density in $Ga_{1-x}Mn_xAs$ are in fact not contradictory. Our study thus provides a consistent experimental picture of the magnetic and electronic properties of $Ga_{1-x}Mn_xAs$.

DOI: 10.1103/PhysRevB.87.205314 PACS number(s): 73.50.−h, 78.20.−e, 75.70.−i, 75.50.Pp

I. INTRODUCTION

Much of the interest in the ferromagnetic semiconductor $Ga_{1-x}Mn_xAs$ stems from the rich physics of metallicity *and* ferromagnetism induced in a semiconducting host through doping with magnetic impurities. There is a general consensus that itinerant holes, introduced by the Mn doping, mediate the ferromagnetic interaction between the magnetic moments of the Mn ions.[1–3] Thus all proposed ferromagnetic (FM) mechanisms of $Ga_{1-x}Mn_xAs$ are intimately tied to the dynamics of the charge carriers. This interplay between the electronic structure and magnetism necessitates studies that can form a comprehensive description of both the observed electronic *and* magnetic properties in a consistent manner. This need is amplified by a long standing controversy regarding the location of Fermi level (E_F) in the band structure of FM $Ga_{1-x}Mn_xAs$ (see reviews by Dietl[4] and/or Samarth,[5] for instance). This controversy centers on the character of the states at E_F, as we describe below.

In one scenario, Zener's double exchange, of which the electronic structure is diagramed in the top panel of Fig. 1(a), E_F resides in the partially occupied majority band of Mn impurity d states. In this picture, electronic conduction via hopping within the impurity band (IB) mediates the magnetic exchange, with an energy gain controlled by the magnitude of the hopping matrix element t for ferromagnetically coupled Mn impurities.[3,6,7] Because this interaction relies on itinerant carriers, there is no energy gain for ferromagnetism if the IB is completely filled or completely empty.

In the alternative Zener's p-d exchange scenario [middle panel of Fig. 1(a)], E_F resides in the exchange split valence p band of the host. In this picture, hybridization of the impurity d wave functions with the p wave functions of the neighboring p elements produce level repulsion of the like spins states. Thus the majority spin p band is shifted to higher energies, and the minority band is shifted to lower energies. This scenario results in a relatively weak, yet very long-ranged interaction that is due to the extended nature of the p states of the host valence band (VB).[1,8]

Double exchange and p-d exchange are not necessarily mutually exclusive scenarios for the true nature of the interatomic exchange interaction. Rather, double exchange and p-d exchange may both contribute to the resultant FM ground state of $Ga_{1-x}Mn_xAs$. In terms of the magnetic interactions, the IB double exchange and the VB p-d exchange scenarios are merely the strong-coupling narrow-band limit, and the weak-coupling extended state limit of each other, respectively. Other magnetic exchange interactions may also play a secondary role as well, but these are beyond the scope of this paper (see reviews of Refs. 1 and 3 for a complete profile of magnetic interactions). The crucial point is that the nature of the interaction depends heavily on details of the electronic structure and degree of localization of the mediating holes.

In this work, we experimentally address both the magnetic and the electronic properties of the prototype dilute magnetic semiconductor $Ga_{1-x}Mn_xAs$ using infrared (IR) spectroscopy. We first examine the relationship between the infrared spectral weight, which is proportional to the carrier density [see Eq. (1)], and the ferromagnetic transition temperature T_C. This relationship is determined through a sum-rule analysis of our data and additional IR data available in the literature (see Refs. 9–11) (see Sec. II). Our analysis shows the position and degree of localization at E_F plays a key role in controlling T_C [see Fig. 1(d) and discussion in Sec. II]. In Sec. IV, we perform a detailed examination of the spectral features observed in the

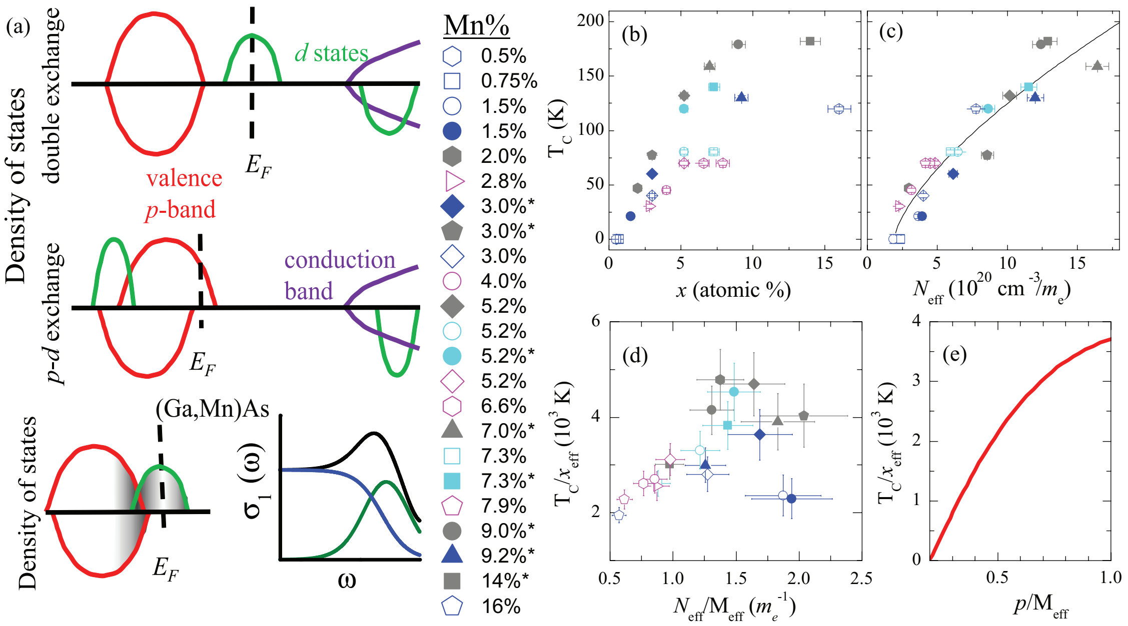

FIG. 1. (Color online) (a) Schematic diagram of the spin-polarized density of states for the case of double exchange (top) and p-d exchange (middle). In the bottom of (a), we show on the left a schematic spin-polarized density of states in the vicinity of E_F for (Ga,Mn)As consistent with our experiments, where gray shaded regions indicate increased localization. The bottom right of (a) is a schematic diagram of the IR conductivity of (Ga,Mn)As, as measured by our experiments. The black curve is the total IR conductivity, whereas the blue curve represents the itinerant carrier response, and the dark green indicates the valence p-band to impurity d-band interband transition contribution to the spectra. For (b)–(e), magenta points are from Ref. 9, cyan from Ref. 10, gray from Ref. 11, and blue from this work (see Table I for additional sample details). The data from Refs. 9 and 10 were collected at 5–7 K, that of Ref. 11 at room temperature, and that of this work, at ~25 K. Open points indicate as-grown films, and filled points indicate that the film was annealed. (b) Ferromagnetic transition temperature T_C as a function of the nominal doping concentration x of $Ga_{1-x}Mn_xAs$ films. (c) T_C as a function of the IR spectral weight $N_{\rm eff}$ [defined in Eq. (1)] of $Ga_{1-x}Mn_xAs$ films. The black line is a best-fit power law trend line with an exponent of 0.67. (d) T_C normalized by the effective Mn concentration $x_{\rm eff}$ as a function of the IR spectral weight $N_{\rm eff}$ normalized by the effective Mn moment $M_{\rm eff}$, as described in the text. (e) Theory of Ref. 12, demonstrating the trend expected in $T_C/x_{\rm eff}$ when the FM properties are calculated in a Zener p-d exchange framework.

IR data of our $Ga_{1-x}Mn_xAs$ films, and show that these features are also consistent only with a Mn-induced IB scenario and that E_F resides in this region. In this latter section, we discuss a connection between the previous experimental findings of Refs. 10 and 11, which reported seemingly conflicting trends in the peak frequency of a broad mid-IR resonance ω_0 with respect to carrier density. By examining trends in ω_0 with respect to temperature, As:Ga growth ratio, Mn dopant concentration, in both as-grown and annealed samples, our data show that the results of these earlier experiments are in fact not contradictory at all. Moreover, the ω_0 data are consistent with excitations to Mn-induced impurity states.

The samples interrogated in our experiments are grown using a "nonrotated" molecular beam epitaxy (MBE) technique. The nonrotated technique aims to reduce or eliminate As antisite (As_{Ga}) compensation through spatial control of the As-flux during growth (Sec. III). Incorporation of compensating defects is the primary limiting factor in minimizing disorder and maximizing p in $Ga_{1-x}Mn_xAs$. The most prevalent compensating defects are Mn-interstitials (Mn_i), and As-antisites (As_{Ga}), both of which are double donors.[13,14] These defects are an unintentional result of the low growth temperatures necessary to achieve Mn concentrations sufficient for ferromagnetism and to suppress the formation of secondary phases (e.g. MnAs).[15]

Postgrowth annealing at relatively low temperatures has been shown to reduce Mn_i because of their high diffusivity, therefore increasing the hole density p.[16,17] The As_{Ga} defects cannot be removed via annealing at temperatures below 500 °C. Such high annealing temperatures are impractical, however, because at these temperatures, Mn also precipitates out to form MnAs nanoparticles.[18] The necessity for high temperature annealing to reduce AsGa has been circumvented by a "nonrotated" growth technique with spatial control of the As-flux (see Sec. III), which results in a film with a corresponding As_{Ga} gradient.[19] Investigating films grown by this technique, the authors of Ref. 19 have shown that this precise control of the As-flux leads to the systematic reduction (or elimination) of As_{Ga} along the gradient.

The gradient composition of these samples results in a location along the film where As_{Ga} defects have been minimized or eliminated (see Fig. 2). Thus by experimentally probing this optimized location in a film, we obtain data representative of a relatively "clean" sample. Data from the optimized location in our films are reported, for instance, in our analysis of ferromagnetism in Sec. II. Samples grown using the nonrotated technique can provide additional pertinent information through investigation of systematic changes to the IR conductivity spectra, $\sigma_1(\omega)$, of $Ga_{1-x}Mn_xAs$ films along the As:Ga gradient. Tuning the material properties in

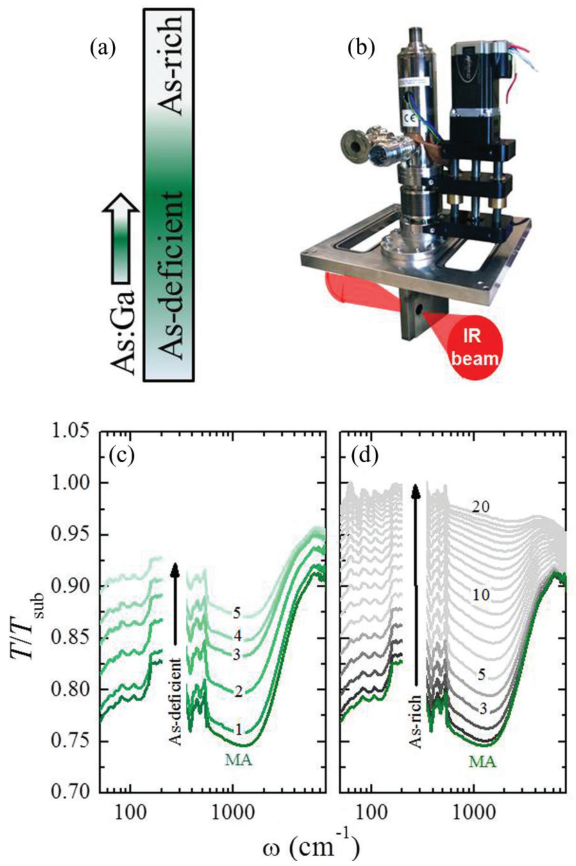

FIG. 2. (Color online) (a) Schematic of our samples with As:Ga gradient. (b) Photograph of our broadband transmission microscope. (c) and (d) Room temperature transmission through the $x = 0.005$ $Ga_{1-x}Mn_xAs$ sample, normalized to transmission of the GaAs substrate. (c) Transmission data taken at 1-mm increments into the As-deficient region of the sample. (d) Transmission spectra taken at 1-mm increments into the As-rich region. Numeric labels indicate the distance in mm from the MA location. The dark green curve displayed in both panels is the transmission spectrum of the MA position.

this manner, and tracking the evolution of the spectroscopic features across the As_{Ga} gradient, yields a detailed picture of the electrodynamics of $Ga_{1-x}Mn_xAs$. Therefore our infrared study, combining an infrared spectral weight analysis of ferromagnetism and the systematic study of the infrared spectral features, serves as a unique endeavor to use a single experimental technique to address both the electronic and magnetic properties of this prototype FM semiconductor.

To further establish that the electrodynamics of FM $Ga_{1-x}Mn_xAs$ is distinct from genuine metallic behavior due to extended states in the host VB, we also examine an $x = 0.009$ $Ga_{1-x}Be_xAs$ sample grown using the same nonrotated technique. This is an ideal system to compare and contrast with the electrodynamics of $Ga_{1-x}Mn_xAs$, as substitutional Be also forms a single acceptor state in GaAs, however, without the accompanying magnetic moment. The $Ga_{0.991}Be_{0.009}As$ sample displays conventional metallicity with spectroscopic features consistent with transport in the host VB, in contrast to that of $Ga_{1-x}Mn_xAs$.

The paper is organized as follows. First, we present our analysis of the relationship between the IR spectral weight and T_C in Sec. II. Following that, we provide details of our samples and experimental methods in Sec. III. Section IV covers the IR conductivity spectra of our p-doped GaAs films, $Ga_{1-x}Mn_xAs$ and $Ga_{1-x}Be_xAs$. This latter section examines the dependence of the spectra on the As:Ga growth ratio in both $Ga_{1-x}Mn_xAs$ and $Ga_{1-x}Be_xAs$, and on the doping dependence in $Ga_{1-x}Mn_xAs$. Discussion of the trends of ω_0 is also found in Sec. IV. Finally, concluding statements are found in Sec. V.

TABLE I. Reference number, nominal doping, film thickness, and ferromagnetic transition temperature for all samples displayed in Fig. 1. "*" indicates samples that have been annealed.

Reference	nominal doping (%)	thickness (nm)	T_C (K)
Ref. 9	2.8	500	30
	4.0	500	45
	5.2	500	70
	6.6	500	70
	7.9	500	70
Ref. 10	5.2	40	80
	5.2*	40	120
	7.3	40	80
	7.3*	40	140
Ref. 11	2.0*	20	47
	3.0*	20	77
	5.2*	20	132
	7.0*	20	159
	9.0*	20	179
	14*	20	182
This work	0.5	200	<4
	0.75	200	<4
	1.5	200	21
	1.5*	200	21
	3.0	200	42
	3.0*	200	60
	9.2*	100	130
	16	100	120

II. AN INFRARED PERSPECTIVE ON TRENDS IN T_C

In Fig. 1(b), we plot T_C as a function of dopant concentration x of all the $Ga_{1-x}Mn_xAs$ samples in our analysis. The samples include as-grown films investigated by Singley *et al.*,[9] as-grown and annealed films of Burch *et al.*,[10] annealed films of Jungwirth *et al.*,[11] and the nonrotated as-grown and annealed samples of this work (see Table I). For the later samples presented in Fig. 1, only the optimized location along the As:Ga gradient is reported in the figure (method for determination of this location is found Sec. IV A). In these works, the total Mn concentration x was determined by electron microprobe analysis (Refs. 9 and 10), measuring the ratio of beam equivalent pressures of Mn and Ga sources before each growth (and cross checked on several samples using secondary ion mass spectroscopy) (see Ref. 11), and growth rate calibrations of MnAs and GaAs reflection high-energy electron diffraction (RHEED) oscillations (this work). The totality of the data in Fig. 1(b) show no clear systematic trend across the doping profile, and nonreproducible T_C for samples of the same nominal dopant concentration. These observations highlight the difficult nature of predicting T_C based on Mn concentration alone in this defect prone material.

The relationship between carrier density and T_C, as opposed to x and T_C, can provide a more insightful picture into the nature of magnetism in this carrier mediated ferromagnet. IR experiments serve as a contactless method sensitive to the carrier density through the sum-rule given by

$$N_{\mathrm{eff}} = \frac{p}{m_{\mathrm{opt}}} = \frac{2}{\pi e^2} \int_0^{\omega_c} \sigma_1(\omega) d\omega. \tag{1}$$

The "spectral weight" N_{eff} is proportional to the effective number of charges contributing to electromagnetic absorption at frequencies below ω_c. Therefore Eq. (1) establishes the relationship between the spectral weight N_{eff} and the charge density p. When Eq. (1) is applied to a feature originating from an interband process, m_{opt} is the reduced mass of the bands involved.[20] When Eq. (1) is applied to a spectral feature arising from an intraband process, m_{opt} is the effective mass of the relevant band. If Eq. (1) is integrated over multiple features arising from distinct processes, m_{opt} will be a "mixture" of the effective masses of each of the excitation processes contributing to the spectrum below ω_c.

In Fig. 1(c), we plot T_C as a function of N_{eff} in the $\mathrm{Ga}_{1\text{-}x}\mathrm{Mn}_x\mathrm{As}$ samples. We use $\omega_c = 6450\ \mathrm{cm}^{-1}$ as the integration cutoff in order to rule out any significant contribution from excitations into the GaAs conduction band. Moreover, this cutoff is well established in these materials and facilitates direct comparison with other studies in the literature.[10,21,22] As can be seen in the figure, while the data do not perfectly collapse onto a single trend line, there is an overall trend indicating that increasing N_{eff} increases T_C. The trend in Fig. 1(b) is indicated by a power-law fit (black line) of all the data points, which finds an exponent of 0.67.

Remarkably, the overall trend in Fig. 1(c) is evident despite the fact that there was no clear trend in T_C versus x [see Fig. 1(b)], and despite the fact that the samples in Fig. 1 span a wide variety of Mn doping levels and growth procedures, including different thicknesses, rotated and nonrotated growths, and as-grown and annealed samples (see Table I). The data of Fig. 1(b) seemingly confirm earlier results of Ref. 17, which also found an empirical relationship between T_C and p in $\mathrm{Ga}_{1\text{-}x}\mathrm{Mn}_x\mathrm{As}$, apparently independent of other physical parameters (though T_C scaled as $\sim p^{1/3}$ rather than $\sim N_{\mathrm{eff}}^{0.67}$ as found here). These earlier results, however, relied on a deconvolution of coupled optical phonon-plasmon modes in Raman spectra. Our result is achieved in a more straightforward manner, as a simple integration of the intragap spectra weight from our IR conductivity. The overall trend in Fig. 1(c) suggests a strong relationship between T_C and p, which is encouraging given that ferromagnetism in $\mathrm{Ga}_{1\text{-}x}\mathrm{Mn}_x\mathrm{As}$ is widely agreed upon to be carrier mediated. Another encouraging aspect of Fig. 1(c) is that up to the largest measured spectral weight ($N_{\mathrm{eff}} > 10^{21}\ \mathrm{cm}^{-3}/m_e$), there are no signs that the trend of increasing T_C is saturating.

One obvious detail missing in any analysis of T_C as a function of p only, such as that described above for the data of Fig. 1(c), is the concentration of Mn moments, which of course are necessary for ferromagnetism. Thus we are interested in estimating the effective Mn concentration x_{eff} of our samples. Out of the total Mn concentration x, the Mn will reside either in substitutional positions or interstitial positions, therefore $x = x_{\mathrm{sub}} + x_i$, where x_{sub} is the concentration of $\mathrm{Mn}_{\mathrm{Ga}}$ and x_i that of Mn_i. Both theory and experiments suggest that Mn_i-$\mathrm{Mn}_{\mathrm{Ga}}$ pairs couple antiferromagnetically,[16,23–27] therefore the effective Mn concentration contributing to ferromagnetic order is then $x_{\mathrm{eff}} = x_{\mathrm{sub}} - x_i$. Mn_i are also considered to be double donors,[13,14] compensating the intentional hole doping of $\mathrm{Mn}_{\mathrm{Ga}}$. Through this latter fact, and by invoking the relationship between the carrier density and the spectral weight established in Eq. (1), we can write that $\frac{a^3}{4} m_{\mathrm{opt}} N_{\mathrm{eff}} = x_{\mathrm{sub}} - 2x_i$, where a is the GaAs lattice constant (for simplicity, we have assumed that the concentration of $\mathrm{As}_{\mathrm{Ga}}$ is zero). Putting these relations together, we arrive at our estimate of effective Mn concentration $x_{\mathrm{eff}} = \frac{1}{3}x + (\frac{2}{3})\frac{a^3}{4} m_{\mathrm{opt}} N_{\mathrm{eff}}$.

For m_{opt} in our equation for x_{eff}, we choose m_{opt} to be in the range of the effective VB mass, placing it from 0.3–0.4 m_e. This choice was guided by IR experiments on (Ga,Mn)As-based electric field effect devices.[28] These latter experiments found, noting that m_{opt} is dominated by the VB mass, the integration limit in the sum rule [see Eq. (1)] is on the order of several thousand wave numbers in (Ga,Mn)As, that Mn doping does not lead to substantial renormalization of the GaAs host VB. This result on field effect devices is in accord with the analysis of resonant tunneling spectroscopy experiments in (Ga,Mn)As layers as well.[29] It is worth noting that the maximum m_{opt} such that $x_{\mathrm{eff}} \leqslant x$ for all the samples in Fig. 1 is $\sim$0.8 m_e. Using this maximum value of m_{opt} does not change the qualitative behavior of the data in Fig. 1(d), which we discuss in the following paragraphs.

Having obtained an estimate of x_{eff}, we plot T_C/x_{eff} versus $N_{\mathrm{eff}}/\mathrm{M}_{\mathrm{eff}}$, where $\mathrm{M}_{\mathrm{eff}}$ is the density of effective Mn moments ($\mathrm{M}_{\mathrm{eff}} = \frac{4}{a^3} x_{\mathrm{eff}}$) in Fig. 1(d). The value of $N_{\mathrm{eff}}/\mathrm{M}_{\mathrm{eff}}$ gives an approximation of the relative degree of compensation of each film. For $N_{\mathrm{eff}}/\mathrm{M}_{\mathrm{eff}} < 1.25\ m_e^{-1}$, these data show a monotonic increase in T_C/x_{eff} for increasing $N_{\mathrm{eff}}/\mathrm{M}_{\mathrm{eff}}$. This general trend is expected in both a p-d exchange scenario,[12] as well a double-exchange scenario[3] for $\mathrm{Ga}_{1\text{-}x}\mathrm{Mn}_x\mathrm{As}$. For $N_{\mathrm{eff}}/\mathrm{M}_{\mathrm{eff}} > 1.25\ m_e^{-1}$, the data seem to be maximized in a range of roughly $1.3\ m_e^{-1} < N_{\mathrm{eff}}/\mathrm{M}_{\mathrm{eff}} < 1.6\ m_e^{-1}$. We note the film with the highest T_C (182 K) falls within this latter range, while the film with the second highest T_C (179 K) falls within the former range. Continuing to higher values of $N_{\mathrm{eff}}/\mathrm{M}_{\mathrm{eff}}$, the data then show either a plateaued or decreasing trend, which is not easily discerned given the error bars. However, the $x = 0.015$ samples show a significant overall decrease in T_C/x_{eff}, displaying a suppression of over 50%, while having among the largest values of $N_{\mathrm{eff}}/\mathrm{M}_{\mathrm{eff}}$.

The theoretical curve of T_C/x_{eff} versus $N_{\mathrm{eff}}/\mathrm{M}_{\mathrm{eff}}$ calculated in Ref. 12 is displayed in Fig. 1(e). This curve is based on an electronic structure, calculated using a microscopic tight-binding approximation in which the valence and impurity bands of $\mathrm{Ga}_{1\text{-}x}\mathrm{Mn}_x\mathrm{As}$ have completely merged. The ferromagnetic properties are thus calculated according to a semiphenomenological p-d exchange mean-field approximation. The key theoretical prediction of Ref. 12, is a systematic, monotonically increasing trend in T_C/x_{eff}, with a corollary that the highest T_C will occur for films with close to zero compensation. Furthermore, to the best of our knowledge, all

VB *p*-*d* exchange descriptions predict a monotonic increase of T_C with both p and x_{eff}.

According to our IR spectral weight analysis, the key prediction made in the *p*-*d* exchange framework (monotonic increase of T_C/x_{eff}) is not in agreement with the data. Nonmonotonic trends of T_C/x_{eff} have also been reported in Ref. 30 using a simultaneous combination of channeling Rutherford backscattering (c-RBS) and channeling particle-induced x-ray emission (c-PIXE).[31] In contrast, high-field Hall measurements of the carrier density do not show the nonmonotonic behavior seen in Fig. 1(d).[12] The experimental data of Refs. 30 and 12 have both been disputed.[31,32] With this noted disagreement in the literature, we emphasize that our experiments are done using a technique entirely different from any of those above. Furthermore, our IR method is a contactless probe, and the sum-rule analysis is based on model-independent arguments that are rooted in the causality of the electromagnetic response.[33] We reiterate that the highest T_C films (182 and 179 K) displayed in Fig. 1 (filled gray square and circle, respectively) have spectral weight that is well below that expected for the uncompensated case, which is contradictory to the predictions of the *p*-*d* exchange mean-field approximation. Therefore we argue that the ferromagnetic properties of $\mathrm{Ga}_{1\text{-}x}\mathrm{Mn}_x\mathrm{As}$ require description beyond Zener's *p*-*d* exchange model.

To our knowledge, there is no microscopic theory that has presented a quantitative description of the nonmonotonic behavior of Fig. 1(d). It was argued in Ref. 30 that T_C is controlled by the location of E_F in a Mn-induced IB. From the basis of tight-binding Anderson calculations, however, IB models used to describe earlier experiments[10,34–36] fail to demonstrate how the IB could remain sufficiently narrow as to avoid overlap with the VB at the doping levels necessary to initiate FM.[37] A strictly detached IB, however, is not theoretically necessary for the qualitative behavior seen in Fig. 1(d). First-principles investigations of the electronic structure and magnetism find $\mathrm{Ga}_{1\text{-}x}\mathrm{Mn}_x\mathrm{As}$ to be an intermediate case, with contributions to ferromagnetism coming from both *p*-*d*-like and double exchange-like mechanisms. The calculated DOS of this later study finds significant merging of the IB and VB, yet still with a large amplitude of d states at E_F, *and* a corresponding suppression of T_C as a function of increased hole concentration.[38] These same techniques when applied to other dilute magnetic semiconductors show the domelike behavior of T_C typical of a double exchange FM mechanism becomes further pronounced in cases where the separation of the IB and VB are more distinct, e.g., $\mathrm{Ga}_{1\text{-}x}\mathrm{Mn}_x\mathrm{N}$.

The nonmonotonic nature of the data of Fig. 1(d) shows that the FM mechanism of $\mathrm{Ga}_{1\text{-}x}\mathrm{Mn}_x\mathrm{As}$ has a strong double-exchange component. This fact highlights the important role played by impurity states and localization at E_F. A schematic representation of the DOS consistent with our data is shown in the bottom panel of Fig. 1(a). Although this schematic lacks subtleties that may vary with parameters such as the Mn concentration and compensation in real materials, a generic optical conductivity line shape [bottom right panel of Fig. 1(a)] has been observed in all FM $\mathrm{Ga}_{1\text{-}x}\mathrm{Mn}_x\mathrm{As}$ samples of the studies represented in Fig. 1. This latter fact implies that the spectroscopic features and carrier dynamics in FM $\mathrm{Ga}_{1\text{-}x}\mathrm{Mn}_x\mathrm{As}$ films reported in the literature originate from the same basic physical picture, despite variations in the growth and film preparation procedures across these works. Furthermore, detailed spectroscopic probes of the IMT in GaMnAs reveal that the generic picture of the DOS in bottom panel of Fig. 1(a) holds over a wide range of Mn concentrations, persisting over an order of magnitude of Mn doping beyond the onset of conduction in FM $\mathrm{Ga}_{1\text{-}x}\mathrm{Mn}_x\mathrm{As}$.[22] In Sec. IV, we expand upon the earlier IR data and further demonstrate that the generic spectral features observed in $\mathrm{Ga}_{1\text{-}x}\mathrm{Mn}_x\mathrm{As}$ persist over a wide parameter space and are consistent with an IB scenario.

III. SAMPLES AND EXPERIMENTAL METHODS

A. Sample growth and characteristics

All films in this study were prepared via MBE, on semi-insulating (001) GaAs substrates. The films were prepared using the nonrotated, low-temperature growth techniques reported in Refs. 19 and 39. Since this study involved several doping regimes, details of the growth vary between samples. Specific details on the film preparation of all samples can be found in Table II. In the $\mathrm{Ga}_{1\text{-}x}\mathrm{Mn}_x\mathrm{As}$ samples, the Mn dopant concentration was determined by growth rate calibrations of MnAs and GaAs RHEED oscillations. For the $\mathrm{Ga}_{0.991}\mathrm{Be}_{0.009}\mathrm{As}$ sample, the Be concentration was determined from room-temperature Hall effect data.

The nonrotated technique utilizes a geometry in which the MBE system provides a continuous variation in the As:Ga ratio in one direction along the wafer. This yields precise control over the density of $\mathrm{As}_{\mathrm{Ga}}$, while holding Mn (or Be) flux approximately constant.[19] Local transport studies along the As:Ga gradient demonstrate that increasing the $\mathrm{As}_{\mathrm{Ga}}$ density reduces the hole density p, mobility, and dc conductivity σ_{dc} in $\mathrm{Ga}_{1\text{-}x}\mathrm{Mn}_x\mathrm{As}$.[19] Additionally, $\mathrm{As}_{\mathrm{Ga}}$ also affects T_C, magnetization, and magnetic hysteresis curves in FM samples.[19,39] These studies show that the location of minimum $\mathrm{As}_{\mathrm{Ga}}$ density, defined by the location of maximum p found along the As:Ga gradient, also corresponds to the region where all of the above properties are optimized. We note, detailed studies of Ref. 19 have concluded full dopant incorporation is not achieved in the As-deficient regions. In the "optimized" and As-rich regimes, however, the data indicate relatively constant Mn concentration (within 0.1%

TABLE II. Sample properties of all the films measured in this study including the dopant concentration, film thickness, growth temperature, and annealing temperature (where applicable). "*" indicates that samples have been annealed.

dopant	(%)	thickness (nm)	growth (°C)	annealing (°C)
Mn	0.5	200	250	. . .
	0.75	200	250	. . .
	1.5	200	250	. . .
	1.5*	200	250	220
	3.0	200	220	. . .
	3.0*	200	220	200
	9.2*	100	200	180
	16	100	150	. . .
Be	0.9	100	250	. . .

variation) along the As:Ga gradient.[19] In the heavily alloyed samples [$x = 0.092^*$ and 0.16 Mn (* indicates the sample was annealed)], this latter statement is only true for a small region near the optimal location.[39]

$Ga_{1\text{-}x}Mn_xAs$ samples of $x = 0.005$, 0.0075 were found to be paramagnetic (PM) at all locations along the films. The other more heavily doped $Ga_{1\text{-}x}Mn_xAs$ films were found to be FM, with T_C in the region of minimized compensating defects (referred to as MA, with this naming convention explained in Sec. III B below) listed in Table II. The $x = 0.015^*$, 0.03^*, and 0.092^* $Ga_{1\text{-}x}Mn_xAs$ samples were also subjected to low-temperature annealing. The $x = 0.015$ and 0.015^* $Ga_{1\text{-}x}Mn_xAs$ films are the same sample pre- and post-annealing; the same is true for the $x = 0.03$ and 0.03^* $Ga_{1\text{-}x}Mn_xAs$ films. In the $x = 0.015^*$ and 0.03^* samples, T_C after annealing was determined by the temperature of maximum low-frequency resistivity [$\rho_{\mathrm{IR}} = 1/\sigma_1(40\ \mathrm{cm}^{-1})$][22] [see Fig. 5(i)]. For all other samples, including $x = 0.015$ and 0.03 before annealing, T_C was measured by SQUID magnetometry.

B. Experimental methods

In order to characterize the effects of the As:Ga gradient on the optical properties, we developed a broadband (far-IR to near-ultraviolet) microscope compatible with low-temperature (∼20 K) operation [see Fig. 2(b)]. Our experimental setup incorporates a 4× beam condenser and linear translation stage in a Fourier transform IR spectrometer to obtain frequency-dependent transmission spectra. The spatial resolution of the apparatus is below 1 mm, which is appropriate for the series of films investigated here. This assertion was validated through direct mid-IR transmission microscopy experiments, with the IR-beam diameter focused to less than 100 μm at the sample, taking measurements in 1 mm increments along the As:Ga gradient. The microtransmission data were supplemented with room-temperature microellipsometry measurements for several films ($x = 0.005$, 0.0075, 0.015, 0.03, 0.16 Mn and $x = 0.009$ Be). The ellipsometry data span a frequency range of 6 000 $\mathrm{cm}^{-1} \leqslant \omega \leqslant 40\,000\ \mathrm{cm}^{-1}$, with spatial resolution ∼150 μm.

Characteristic transmission data along the As:Ga gradient are displayed in Figs. 2(c) and 2(d). The figures show room-temperature transmission through the $x = 0.005$ $Ga_{1\text{-}x}Mn_xAs$ sample, normalized to that of the GaAs substrate. We identify the location of maximum p, as the position corresponding to the maximum absorption along the sample, and thus refer to this location as MA. A more rigorous and quantitative determination of the location of maximum p is completed via optical sum rules (1), as detailed later in the manuscript (see Sec. IV A). With this definition of the MA point, the spectra can be divided into two regimes: As-rich and As-deficient. Spectra in the As-deficient regime show a rapid increase in overall transmission as the IR probe moves deeper into the deficient regime. Detailed studies reported in Ref. 19 have concluded that full dopant incorporation is not achieved in the As-deficient regions. A reduction in dopant concentration is consistent with the decreased absorption observed. Thus the IR studies in this work focus on the As-rich and MA positions of the samples. In these latter locations, a systematic increase in the overall transmission is observed as the IR beam is moved from MA deeper into the As-rich region. The increase of transmission in the As-rich regime is consistent with reduction in p due to As_{Ga} compensation.

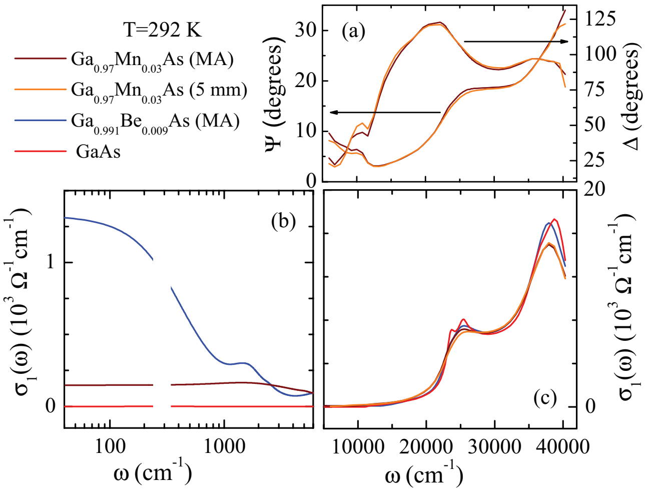

FIG. 3. (Color online) Panel a shows the ellipsometric angles Ψ and Δ for the $x = 0.03$ $Ga_{1\text{-}x}Mn_xAs$ for MA and 5 mm into the As-rich region. The angle of incidence for data in (a) was 75°. The $\sigma_1(\omega)$ spectra of the $x = 0.03$ $Ga_{1\text{-}x}Mn_xAs$ film, the $Ga_{0.991}Be_{0.009}As$ film, and pristine GaAs in the intragap region are shown in (b), and extending beyond the GaAs band gap in (c). (c) additionally displays the spectrum of the $x = 0.03$ $Ga_{1\text{-}x}Mn_xAs$ 5 mm into the As-rich region. The $\sigma_1(\omega)$ data are obtained by a simultaneous fitting of transmission and ellipsometric data, as described in the text.

Spectroscopic data at frequencies beyond the fundamental GaAs band gap were obtained via ellipsometry measurements. Ellipsometry measures the ratio of the complex reflectivity coefficient (r) of s- and p-polarized light. The experimental observables are the ellipsometric angles Ψ and Δ according to

$$\frac{r_p}{r_s} = \tan(\Psi)e^{i\Delta}, \tag{2}$$

where the subscripts p and s denote the incident polarization. Figure 3(a) shows representative data of our microellipsometry experiments for the $x = 0.03$ $Ga_{1\text{-}x}Mn_xAs$ film at the MA position.

To develop a quantitative understanding of the optical data, it is instructive to express our observables in terms of the complex IR conductivity spectrum $\sigma(\omega) = \sigma_1(\omega) + i\sigma_2(\omega)$. We extract the complex conductivity spectrum from our optical data via multioscillator modeling. For this model, we use only Kramers-Kronig (KK) consistent oscillators and perform a simultaneous fitting of both the transmission and ellipsometric data. In this way, we construct a KK consistent model of $\sigma(\omega)$ over the entire experimental range. Modeling the data over such a large experimental frequency range assures a high degree of confidence in the uniqueness and accuracy of each experimental fit.[40,41] We focus on the real part of the conductivity spectrum, $\sigma_1(\omega)$, describing the dissipative processes in the system. Figures 3(b) and 3(c) display representative plots illustrating $\sigma_1(\omega)$ extracted by the simultaneous fitting of the room-temperature transmission spectrum and ellipsometric data as described above. The data are displayed for the $Ga_{0.97}Mn_{0.03}As$ and $Ga_{0.991}Be_{0.009}As$ samples at MA, both in the intragap region [see Fig. 3(b)] as well as frequencies extending above the fundamental GaAs band gap [see Fig. 3(c)]. Further discussion of the spectroscopic features in the intragap regime are found in Sec. IV.

IV. INTRAGAP RESPONSE OF *p*-DOPED GALIUM ARSENIDE

A. Carrier density gradient

Figures 4(a)–4(d) show representative transmission spectra and corresponding $\sigma_1(\omega)$ for the $Ga_{0.97}Mn_{0.03}As$ and $Ga_{0.991}Be_{0.009}As$ samples. These panels highlight the equivalence of the location along the As:Ga gradient of maximum absorption in the transmission spectra to that of the maximum in overall $\sigma_1(\omega)$. Therefore the MA location can be determined by the position along the As:Ga gradient that displays the maximum spectral weight [see Eq. (1)]. Figures 4(e)–4(h) show the intragap $\sigma_1(\omega)$ data of the other gradient samples measured in this study. Data along the As:Ga gradient of the heavily alloyed samples ($x = 0.09$ and 0.16 $Ga_{1\text{-}x}Mn_xAs$) are not reported because it has been determined that quality surfaces and interfaces are only found in a narrow region near MA.[39] The effect of the As:Ga gradient in terms of the spatial location is quantified in Fig. 4(i) by the spectral weight N_{eff}, normalized to N_{eff} at MA for each sample [absolute scale for N_{eff} can be read off of Fig. 6(c)]. Figure 4(i) demonstrates suppression of N_{eff} as As content increases past the optimal concentration to be a generic result for the *p*-doped GaAs samples of this study.

Figures 4(a)–4(h) demonstrate that the qualitative features of the spectra, although different for Be and Mn-doped samples, are not radically modified by additional As_{Ga} compensation. $Ga_{1\text{-}x}Mn_xAs$ $\sigma_1(\omega)$ spectra, both at MA and several millimeters into the As-rich regime, reveal a line shape consisting of a broad mid-IR resonance and relatively flat conductivity in the far IR. In the $Ga_{1\text{-}x}Be_xAs$ data of in Fig. 4, the spectra at MA and in the As-rich region are dominated by a pronounced low-frequency response. This latter peak can be modeled semiclassically as a Drude peak, given by

$$\sigma_1(\omega) = \frac{\sigma_{\text{dc}}}{1 + \tau^2\omega^2}. \qquad (3)$$

The Drude peak is characteristic of a free carrier response in a metal or degenerate semiconductor, with the amplitude equal to the dc conductivity σ_{dc} and the width of the peak quantifying the free carrier scattering rate $1/\tau$. As can be seen in the figure, the increase of As_{Ga} in the As-rich region of $Ga_{1\text{-}x}Be_xAs$ suppresses the Drude conductivity and broadens the Drude width. A narrow mid-IR resonance is also suppressed and broadened in the As-rich regions.

B. Doping dependence

The temperature dependence of $\sigma_1(\omega)$ for all the $Ga_{1\text{-}x}Mn_xAs$ samples in this study at MA are shown in Fig. 5. We observe a qualitatively similar line shape at all Mn dopings x [see Fig. 1(a)]. The far-IR conductivity, attributed to the itinerant carrier response, is nearly completely suppressed at the lowest temperatures in the PM samples ($x < 1\%$). This vanishing conductivity supports the notion that these samples reside on the insulating side of the $Ga_{1\text{-}x}Mn_xAs$ insulator-to-metal transition (IMT). In these insulating samples, the observed broad mid-IR resonance in the vicinity of Mn-acceptor binding energy has a natural assignment of VB to IB transitions.

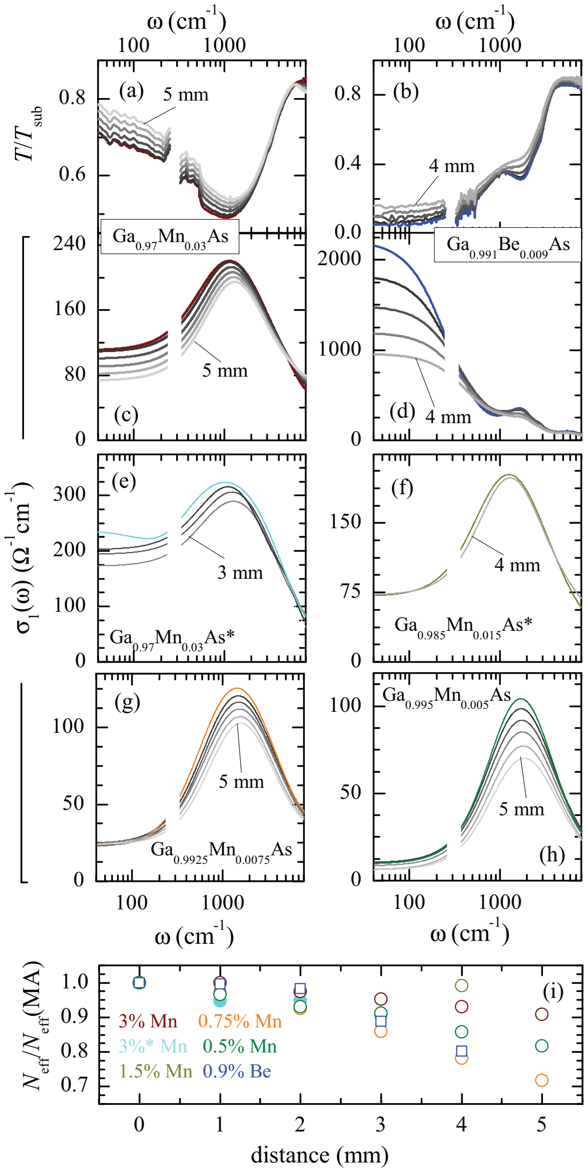

FIG. 4. (Color online) (a) and (b) Transmission data normalized to the GaAs substrate taken at 20 K for the $x = 0.03$ $Ga_{1\text{-}x}Mn_xAs$ and $Ga_{0.991}Be_{0.009}As$ samples, respectively. (c) and (d) The corresponding $\sigma_1(\omega)$ spectra for the $x = 0.03$ $Ga_{1\text{-}x}Mn_xAs$ and $Ga_{0.991}Be_{0.009}As$ samples, respectively. The data are displayed at the MA point, which appear in color, and at 1-mm increments into As-rich region appearing in gray scale (increasingly lighter with distance from MA). The breaks in the data near 300 cm^{-1} are due to a GaAs phonon. The low-temperature $\sigma_1(\omega)$ spectra for the $x = 0.005$, 0.0075, 0.015, 0.015*, and 0.03* $Ga_{1\text{-}x}Mn_xAs$ films at MA, and 1-mm increments into the As-rich region are shown in (e)–(h). (i) The spectral weight N_{eff} [see Eq. (1)] as a function of distance from the MA point, normalized to N_{eff} at MA for the data displayed in (c)–(h).

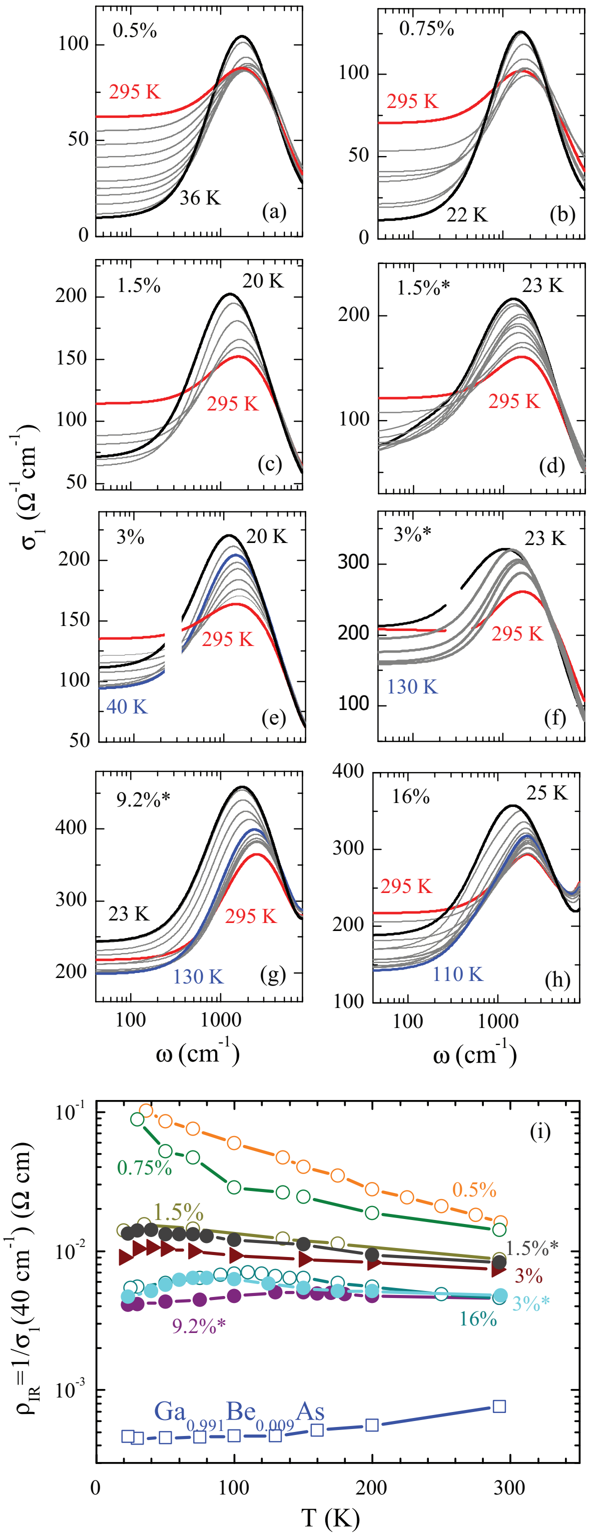

FIG. 5. (Color online) (a)–(h) The temperature dependence of the $\sigma_1(\omega)$ spectra (at MA) for all of our $Ga_{1\text{-}x}Mn_xAs$ films. Room-temperature spectra are shown in red, the lowest temperature spectra are in black, and the minima in conductivity near $T = T_C$ are in blue. All other temperatures are shown in gray for clarity. The breaks in the data near 300 cm^{-1} are due to a GaAs phonon. (i) The temperature dependence of ρ_{IR} (defined in the text) for all the samples at the MA position.

The persistence of the far-IR conductivity down to the lowest temperatures in $Ga_{1\text{-}x}Mn_xAs$ samples of $x > 0.0075$ reveals films in this dopant regime to be beyond the onset of conduction. However, the onset of conduction in $Ga_{1\text{-}x}Mn_xAs$ remains distinct from genuine metallicity, as can be seen in Fig. 5(i). In this panel, we plot the temperature dependence of the "infrared resistivity" [$\rho_{IR} = 1/\sigma_1(40\ \mathrm{cm}^{-1})$]. The data in the dilute Mn-doped samples ($x = 0.005, 0.0075$) show the systematic increase in ρ_{IR} expected in the case of thermally activated transport. The insulating behavior of these samples down to the lowest temperatures measured establishes the $Ga_{1\text{-}x}Mn_xAs$ films in this doping regime as below the onset of conduction.

The onset of conduction is marked by the finite σ_{dc} in the limit of ω, $T \to 0$, exhibited by the $Ga_{1\text{-}x}Mn_xAs$ films of $x > 0.0075$. Nevertheless, the ρ_{IR} of the films in this latter dopant regime still display signs of activated transport above T_C. The onset of ferromagnetism radically alters the temperature dependence of $\sigma_1(\omega)$ and ρ_{IR}, as below T_C the activated character is reversed. An anomalous increase of the low-energy spectral weight with the development of magnetization has also been demonstrated in earlier work on $Ga_{1\text{-}x}Mn_xAs$,[9,22,42] $In_{1\text{-}x}Mn_xAs$,[43] as well as a canonical double-exchange material $La_{1\text{-}x}Sr_xMnO_3$.[33,44] This "mixed" behavior of insulating and metallic trends underscores the unconventional nature of conduction in Mn-doped GaAs beyond the IMT boundary, and serves as a signature of the deep bond between magnetism and the carrier dynamics. Moreover, it establishes the distinction between the onset of conduction and genuine metallicity, the latter of which we now describe below for $Ga_{0.991}Be_{0.009}As$.

The room-temperature spectrum of $Ga_{0.991}Be_{0.009}As$ [blue curve in Fig. 3(c)] reveals a pronounced Drude peak and a narrow mid-IR resonance. Upon cooling to 25 K, the Drude peak sharpens and increases in amplitude, typical of genuinely metallic behavior, as does the mid-IR resonance [compare blue curves of Figs. 3(b) and 4(d)]. The temperature dependence of ρ_{IR} for this film reveals a metallic trend throughout the entire measured temperature range [see Fig. 5(c)]. The pronounced Drude peak and metallic temperature dependence establish the genuine metallicity of this film, in contrast with the mixed behavior of $Ga_{1\text{-}x}Mn_xAs$ beyond the onset of conduction. Furthermore, much weaker far-IR spectral weight is found in Mn-doped samples than that of the Be-doped film.[22]

The carrier density can be readily measured by the Hall effect in the nonmagnetic $Ga_{0.991}Be_{0.009}As$ system. From this fact, and coupled with the prominent Drude peak, the effective carrier mass can be determined from Eq. (1). This effective mass was found to be $0.29m_e$ at MA for the $Ga_{0.991}Be_{0.009}As$ sample. This value of the carrier mass is supported by the mass extracted from mobility data of p-type GaAs doped with nonmagnetic (Zn, C, or Be) acceptors.[45] Moreover, is in good agreement with the two-band transport mass of light and heavy holes in the GaAs VB of $0.38m_e$.[46] The combination of the light effective carrier mass and metallic temperature dependence of the Drude peak are strong evidence that the IR spectra of the $Ga_{0.991}Be_{0.009}As$ film are representative of the IR response of carriers that reside in extended states of the GaAs host VB.

Decoupling the delocalized Drude-like contributions to the spectra from interband transition contributions limit analysis similar to that above for estimating carrier masses in $Ga_{1-x}Mn_xAs$. However, reasonable estimates reveal the effective mass of carriers in $Ga_{1-x}Mn_xAs$ to be significantly larger than that of the metallic Be-doped sample. The large mass of charge carriers in $Ga_{1-x}Mn_xAs$ are apparent from the much weaker far-IR spectral weight in $Ga_{1-x}Mn_xAs$ samples with similar doping to that of the Be-doped film. We further note that the weak far-IR spectral weight of $Ga_{1-x}Mn_xAs$ samples extends to films with over an order of magnitude higher dopant concentration than the $Ga_{0.991}Be_{0.009}As$ film. More detailed quantitative analysis of $Ga_{1-x}Mn_xAs$ effective masses in IR data can be found in Refs. 10 and 47. The relatively large carrier mass is indicative of transport within a narrow band of impurity character. Moreover, the weak far-IR conductivity and coexistence of insulating and metallic trends in the temperature dependence establish that descriptions of electronic conduction in $Ga_{1-x}Mn_xAs$ require an emphasis on localization. These latter characteristics are distinct from extended states in the VB and are in line with proposed theories of IR conductivity of $Ga_{1-x}Mn_xAs$.[48,49]

C. Mid-IR peak

In the discussion above, we demonstrated the notable differences in the far-IR behavior of the spectrum of $Ga_{0.991}Be_{0.009}As$ to that of $Ga_{1-x}Mn_xAs$. Thus it is interesting to note there is a mid-IR resonance in $Ga_{0.991}Be_{0.009}As$ with center frequency similar to that of the broad resonance observed in the $Ga_{1-x}Mn_xAs$ spectra. We argue, however, these features stem from different origins. To highlight the difference between the mid-IR feature in $Ga_{0.991}Be_{0.009}As$ and that of $Ga_{1-x}Mn_xAs$, we plot "scaled" conductivity spectra (of the MA location) in Fig. 6(a). The figure shows $\sigma_1(\omega)$ normalized along the y axis by the value of the conductivity at the peak frequency (ω_0) of the broad mid-IR resonance in the $Ga_{1-x}Mn_xAs$, and the narrow mid-IR resonance in $Ga_{0.991}Be_{0.009}As$ film, respectively. Along the x axis, the spectra are normalized by ω_0 of each film.

The data in Fig. 5 demonstrate that all the Mn-doped samples (both in the insulating regime and those past the onset of conductivity) show very broad, structureless resonances at mid-IR frequencies. Furthermore, upon scaling of these data [see Fig. 6(a)], the Mn-doped samples reveal a nearly identical line shape, barring small nonmonotonic differences in the width of the mid-IR resonance. The similar line shape suggests a similar origin of the mid-IR resonance in both insulating and conducting samples (VB to IB optical excitations).

The persistence of the mid-IR resonance in $Ga_{1-x}Mn_xAs$ samples on the insulating side of the IMT, where an IB is expected for $Ga_{1-x}Mn_xAs$ and noncontroversial,[51,52] to samples well above the onset of conductivity, is key evidence that impurity states maintain a prominent role in FM $Ga_{1-x}Mn_xAs$. We add to this evidence by calculating the $\sigma_1(\omega)$ line shape for VB to IB transitions in $Ga_{1-x}Mn_xAs$ according to the quantum defect method for band-to-acceptor transitions[53] [black dashed line in Fig. 6(a)]. This model was previously applied to absorption in semiconductors by Bebb *et al.*,[54] and later used to model absorption in magnetic semiconductors such as $Cd_{1-x}Mn_xTe$[55] and $Ga_{1-x}Mn_xAs$.[56] The details of our calculation can be found in Ref. 22. Evident in Fig. 6(a) is that the line shape calculated by the quantum defect method is in good agreement with the line shape of the mid-IR resonance observed in the $Ga_{1-x}Mn_xAs$ samples. More complex calculations of VB to IB transitions in $Ga_{1-x}Mn_xAs$ have also been shown to capture key aspects of the experimentally observed mid-IR resonance, see Refs. 48 and 49. Thus the agreement of theoretical calculations and the experimental reality support the assignment of the mid-IR resonance of $Ga_{1-x}Mn_xAs$ to VB to IB excitations.

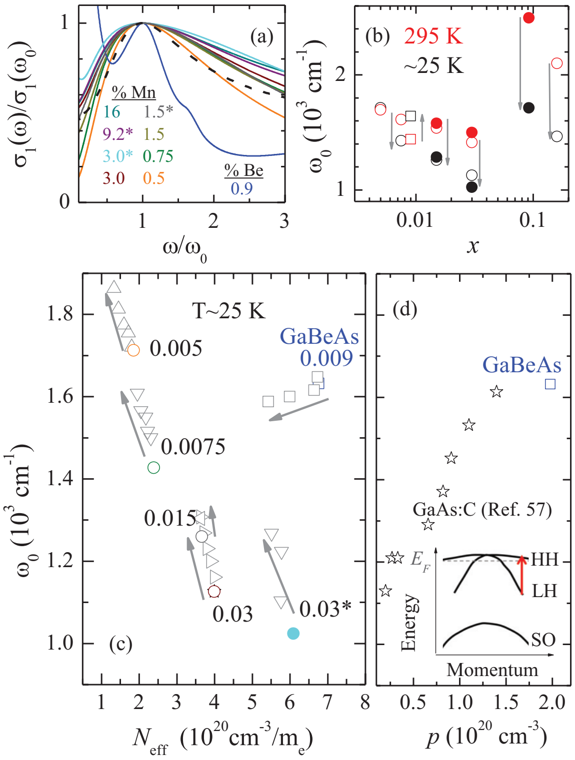

FIG. 6. (Color online) (a) $\sigma_1(\omega)$ normalized along the y axis by the value of the conductivity at the peak frequency (ω_0) of the broad mid-IR resonance in the $Ga_{1-x}Mn_xAs$, and the narrow mid-IR resonance in $Ga_{0.991}Be_{0.009}As$ film, respectively. Along the x axis, the spectra are normalized by ω_0 of each film. The black dashed line shows the scaled $\sigma_1(\omega)$ of VB to IB transitions in $Ga_{1-x}Mn_xAs$ calculated by the quantum defect method, as described in the text. (b) Location of MIR peak ω_0 as a function of doping x. Filled circles in (a) denote annealed $Ga_{1-x}Mn_xAs$ samples, while open circles indicate as-grown $Ga_{1-x}Mn_xAs$ films. The open squares are the data for the $Ga_{0.991}Be_{0.009}As$ sample. The red data points represent room-temperature values, while black points indicate low-temperature data (~25 K). Grey arrows indicate direction of frequency shift upon cooling. (c) Location of ω_0 as a function of N_{eff} as defined by Eq. (1). The gray arrows indicate direction of increase in As_{Ga} compensation. The gray points indicate As-rich positions, colored points the MA position, and the filled circle denotes the sample has been annealed. (d) ω_0 as a function of p for the GaAs:C films from Ref. 50, as well as the MA position of the $Ga_{0.991}Be_{0.009}As$ film at 20 K. The inset shows the valence band structure of GaAs, with the red arrow indicating excitations attributed to the mid-IR peak in the $Ga_{0.991}Be_{0.009}As$ data and GaAs:C data of Ref. 50.

In contrast to the broad resonance observed in the $Ga_{1-x}Mn_xAs$ films, Fig. 6(a) shows the mid-IR resonance observed in $Ga_{0.991}Be_{0.009}As$ is much narrower and has a two-peak structure. The second peak appears as a shoulder on the right-hand side of the main peak, seen near $\omega/\omega_0 = 1.5$ in Fig. 6(a). The frequency position of the two-peak structure is an order of magnitude higher than the Be acceptor binding energy.[57] However, this structure is near the energy expected for intra-VB transitions, in accord with E_F located deep within the VB. The main peak is thus attributed to light-hole band (LH) to heavy-hole band (HH) excitations,[50] while the shoulder is due to excitations from the split-off band (SO)[58] [see Fig. 6(d)].

The peak frequency ω_0 of the broad mid-IR resonance in $Ga_{1-x}Mn_xAs$, and narrow mid-IR resonance in $Ga_{1-x}Be_xAs$, are plotted in Fig. 6 as a function of doping [see Fig. 6(b)] (at MA location only) and N_{eff} [see Fig. 6(c)] (gradient data included). Earlier IR studies of $Ga_{1-x}Mn_xAs$ revealed a systematic redshift of ω_0 as a function of effective carriers.[9,10] However, other more recent experiments have reported ω_0 to blueshift with increased Mn-doping.[11] We note that data reported in Ref. 11 were taken at room temperature, adding some ambiguity to a direct comparison to the 7-K data of Ref. 10. The difficulty in comparing room-temperature and low-temperature data is highlighted in Fig. 6(b). The figure shows that when $Ga_{1-x}Mn_xAs$ samples are cooled from room temperature to low temperature (∼25 K), ω_0 has a pronounced redshift. This latter trend holds true for all the $Ga_{1-x}Mn_xAs$ samples except the lowest doped, insulating paramagnetic $x = 0.005$ sample, which shows virtually no change in ω_0 upon cooling. The exact opposite trend is seen in $Ga_{1-x}Be_xAs$, where a small blue shifts of ω_0 is observed upon cooling from room to low temperature.

In our $Ga_{1-x}Mn_xAs$ samples, considering first only the MA location, the data do not show a singular red- or blueshift trend of ω_0 over the entire doping range measured. Starting with the most dilute Mn-doped samples, the data in Fig. 6(b) show that ω_0 appears to redshift as the doping is increased, both at room and low temperatures. However, there is a large deviation of the redshift trend when the doping is extended to $Ga_{0.908}Mn_{0.092}As^*$ and $Ga_{0.84}Mn_{0.16}As$. Frequency shifts of ω_0 between $Ga_{1-x}Mn_xAs$ samples in an IB scenario are not dependent just on the nominal doping, but the values of p, and p/x as well.[48,49] These latter facts, coupled with the systematic temperature dependence of ω_0, may indicate why trends in ω_0 versus x are nonuniversal, and why relative red- or blueshifts may be found without these results being contradictory. We note that by changing p while holding x constant, E_F may be tuned without otherwise altering the electronic structure (at least to lowest-order approximation). Thus we point out that there are two techniques for changing p while holding x constant from our data: via annealing and via As:Ga gradient. The effects of annealing and of the As:Ga gradient on ω_0 are discussed in the following paragraphs.

We examine the effect of annealing $Ga_{1-x}Mn_xAs$ on ω_0, focusing on the MA location. The $x = 0.015$ sample data show very small change in N_{eff} after annealing (∼7% increase). This small change in N_{eff} is consistent with the assertion of a low degree of compensation in samples in doping regimes below a few atomic percent. Additionally, after annealing the $x = 0.015$ sample shows no significant change in ω_0. However, N_{eff} in the $x = 0.03$ Mn-doped sample was significantly enhanced after annealing (∼54% increase). If we compare only the room-temperature spectra of this latter film, ω_0 in the $x = 0.03$ Mn-doped sample exhibits a blueshift after annealing. This blueshift is consistent with findings on room-temperature spectra of samples pre- and postannealing in Ref. 11. However, if instead only the low-temperature data of this film is compared, the ω_0 data of the $x = 0.03$ Mn-doped sample redshifts after annealing. These low-temperature results are consistent with the 7-K data in Ref. 10. Thus the trends in annealing induced shifts of ω_0 in the $x = 0.03$ $Ga_{1-x}Mn_xAs$ sample are opposite when room-temperature data are compared as to when low-temperature data are compared. This latter fact underscores the difficulty in comparing trends in ω_0 taken at room temperature to that of low temperatures. Furthermore, it emphasizes that the results of Refs. 10 and 11 are not contradictory.

Turning to Fig. 6(c), in each $Ga_{1-x}Mn_xAs$ sample where N_{eff} is tuned by As_{Ga} compensation due to nonrotated growth, a systematic redshift of ω_0 is observed as N_{eff} is increased. Again, the exact opposite trend is observed in $Ga_{1-x}Be_xAs$, where ω_0 blueshifts as N_{eff} is increased. The blueshift trend in $Ga_{1-x}Be_xAs$ is consistent with that of GaAs:C, another p-doped GaAs material determined to be metallic, with conduction occurring in the VB of the host[50] [see Fig. 6(c)]. Unfortunately, similar gradient data are not available on the heavily alloyed Mn-doped samples due to the nature of their growth (see Sec. III).

The observed redshift of ω_0 in $Ga_{1-x}Mn_xAs$ samples upon annealing and As_{Ga} reduction is all in accord with detailed theoretical calculations of $\sigma_1(\omega)$ of $Ga_{1-x}Mn_xAs$ near the onset of conduction in an "IB scenario."[48,49] We emphasize that the opposite trend (blue shift) with respect to carrier density was observed in the "VB metals" $Ga_{1-x}Be_xAs$ and GaAs:C, which is consistent with expectations for p-doped GaAs with E_F within the VB.[10] Although it has been shown that theoretically the screening of disorder could result in redshift of ω_0 as x and p are increased in a VB scenario,[52] experimentally, the trends in ω_0 observed are inconsistent with those observed for VB metals. We cannot fully account for the change in trend of ω_0 in heavily alloyed Mn-doped samples, therefore we only speculate that more detailed calculations of the electronic structure of the VB and IB in heavily alloyed samples may be needed. A final note in this regard is that the low-temperature data show ω_0 is never at significantly higher energy than that of the dilutely Mn-doped $x = 0.005$ sample. This latter fact, in addition to the near identical line shape, further suggests that the mid-IR resonance of the heavily alloyed samples is of the same nature of that of the lower-doped $Ga_{1-x}Mn_xAs$ films.

V. CONCLUSION AND OUTLOOK

The totality of our data demonstrate that neither the electronic nor the magnetic properties of $Ga_{1-x}Mn_xAs$ are in complete accord with expectations of a p-d exchange picture. Instead, the data are suggestive that a Mn-induced IB plays an important role in determining the electronic and magnetic properties. Throughout the text, we have provided arguments and references to relevant theory that supports an IB description for our data. Furthermore, the conclusion of the presence of a Mn-induced IB is supported by numerous previous studies of the electronic structure in FM $Ga_{1-x}Mn_xAs$.[2,10,22,28,29,35,56,59–61]

Nonetheless, despite the experimental and theoretical support for an IB picture $Ga_{1-x}Mn_xAs$ mentioned above, the experimental reality of the precise degree of separation between, and "mixing" of, impurity and valence states remains unresolved. An analysis of resonant tunneling experiments has supported a strictly detached IB with remarkably little exchange splitting of the VB.[29,61] The interpretation of these tunneling data, however, has not been universally accepted (see Ref. 62 for alternative interpretation and Ref. 63 for a response.) Additionally, it is difficult to reconcile a completely detached IB with the fact that there seems to be no cases where reduction of Mn_i by annealing (or reduction of As_{Ga} by nonrotated growth) results in decreased T_C or conductivity. Decreases in these observables are also conspicuously absent when holes are added by the electric field effect in (Ga,Mn)As-based devices.[64] These facts suggest that there is significant overlap of impurity and valence states. Some overlap of these states is also supported by spectroscopic scanning tunneling microscopy experiments, which do not find features consistent with a weakly disorder VB or distinct IB picture, but instead, highlight the importance of compensation and disorder in $Ga_{1-x}Mn_xAs$.[65]

We reiterate that the results of first-principles investigations show that some overlap of valence and impurity states is not in conflict with our results or conclusions. For instance, the first-principles investigations conclude there is a significant double-exchange contribution, in addition to *p*-*d* exchange, to the FM state in $Ga_{1-x}Mn_xAs$ for theoretically uncompensated samples.[3] The spectroscopic data we report here and, in particular, the far-IR response, as well as the nonmonotonic trends of T_C of Fig. 1(d), point towards an emphasis on localization. Thus it seems that a general description of the properties of $Ga_{1-x}Mn_xAs$ requires not just a quantitative picture of the DOS, but also a mobility landscape that quantitatively describes the degree of localization of states in the vicinity of E_F. The details of these landscapes will likely be dependent on x, the concentration and type of compensation, other sources of disorder, and include possible electron-electron interactions.[65]

As stated in the introduction, both double exchange and *p*-*d* exchange may contribute to the resultant FM ground state of $Ga_{1-x}Mn_xAs$. Understanding how these mechanisms compete and or cooperate as the DOS, localization of states, and general character of the states near E_F evolve as the relevant parameters of $Ga_{1-x}Mn_xAs$ are tuned should be vital to a thorough description of this material. Moreover, such an understanding has implications for the broader class of dilute magnetic semiconductors, potentially providing insight into driving future spin-related technology. In any case, our experiments demonstrate that localization and the role of impurity states cannot be neglected in describing the properties of $Ga_{1-x}Mn_xAs$ samples across a wide range of doping and growth conditions. This includes samples doped below the onset of FM, to those with very high T_C (in the context of $Ga_{1-x}Mn_xAs$), as well as samples doped below the IMT, to those far beyond the onset of conduction.

ACKNOWLEDGMENTS

Work at UCSD is supported by the Office of Naval Research. Work at UCSB is supported by the Office of Naval Research and the National Science Foundation. Parts of this work were performed at the Center for Integrated Nanotechnologies, a US Department of Energy, Office of Basic Energy Sciences user facility.

---

[*] Center for Spintronics and Quantum Computation, University of California-Santa Barbara, California 93106, USA (address where work was completed) and Naval Research Laboratory, Washington, DC 20375, USA (current address).

[1] T. Jungwirth, J. Mašek, J. Kučera, and A. H. MacDonald, Rev. Mod. Phys. **78**, 809 (2006).

[2] K. S. Burch, D. D. Awschalom, and D. N. Basov, J. Magn. Magn. Mater. **320**, 3207 (2008).

[3] K. Sato, J. Kudrnovský, P. H. Dederichs, O. Eriksson, I. Turek, B. Sanyal, G. Bouzerar, H. Katayama-Yoshida, V. A. Dinh, T. Fukushima *et al.*, Rev. Mod. Phys. **82**, 1633 (2010).

[4] T. Dietl, Nat. Mater. **9**, 965 (2010).

[5] N. Samarth, Nat. Mater. **11**, 360 (2012).

[6] P. W. Anderson, Solid State Phys. **14**, 99 (1963).

[7] B. L. Sheu, R. C. Myers, J.-M. Tang, N. Samarth, D. D. Awschalom, P. Schiffer, and M. E. Flatte, Phys. Rev. Lett. **99**, 227205 (2007).

[8] T. Dietl, H. Ohno, F. Marsukura, J. Cibert, and D. Ferrand, Science **287**, 1019 (2000).

[9] E. J. Singley, R. K. Kawakami, D. D. Awschalom, and D. N. Basov, Phys. Rev. Lett. **89**, 097203 (2002).

[10] K. S. Burch, D. B. Shrekenhamer, E. J. Singley, J. Stephens, B. L. Sheu, R. K. Kawakami, P. Schiffer, N. Samarth, D. D. Awschalom, and D. N. Basov, Phys. Rev. Lett. **97**, 087208 (2006).

[11] T. Jungwirth, P. Horodyská, N. Tesarová, P. Němec, J. Šubrt, P. Malý, P. Kužel, C. Kadlec, J. Mašek, I. Němec *et al.*, Phys. Rev. Lett. **105**, 227201 (2010).

[12] T. Jungwirth, K. Y. Wang, J. Mašek, K. W. Edmonds, Jürgen König, Jairo Sinova, M. Polini, N. A. Goncharuk, A. H. MacDonald, M. Sawicki, A. W. Rushforth, R. P. Campion, L. X. Zhao, C. T. Foxon, and B. L. Gallagher, Phys. Rev. B **72**, 165204 (2005).

[13] S. C. Erwin and A. G. Petukhov, Phys. Rev. Lett. **89**, 227201 (2002).

[14] M. Missous, J. Appl. Phys. **75**, 3396 (1994).

[15] H. Ohno, A. Shen, F. Matsukura, A. Oiwa, A. Endo, S. Katsumoto, and Y. Iye, Appl. Phys. Lett. **69**, 363 (1996).

[16] K. Edmonds, P. Boguslawski, K. Wang, R. Campion, S. Novikov, N. Farley, B. Gallagher, C. Foxon, M. Sawicki, T. Dietl *et al.*, Phys. Rev. Lett. **92**, 037201 (2004).

[17] K. C. Ku, S. J. Potashnik, R. F. Wang, S. H. Chun, P. Schiffer, N. Samarth, M. J. Seong, A. Mascarenhas, E. Johnston-Halperin, R. C. Myers *et al.*, Appl. Phys. Lett. **82**, 2302 (2003).

[18] J. D. Boeck, R. Oesterholt, and A. V. Esch, Appl. Phys. **68**, 2744 (1996).

[19] R. C. Myers, B. L. Sheu, A. W. Jackson, A. C. Gossard, P. Schiffer, N. Samarth, and D. D. Awschalom, Phys. Rev. B **74**, 155203 (2006).

[20] M. Dressel and G. Grüner, *Electrodynamics of Solids* (Cambridge University Press, Cambridge, MA, 2002).

[21] J. Sinova, T. Jungwirth, S.-R. Eric Yang, J. Kučera, and A. H. MacDonald, Phys. Rev. B **66**, 041202 (2002).

[22] B. C. Chapler, R. C. Myers, S. Mack, A. Frenzel, B. C. Pursley, K. S. Burch, E. J. Singley, A. M. Dattelbaum, N. Samarth, D. D. Awschalom *et al.*, Phys. Rev. B **84**, 081203 (2011).

[23] J. Blinowski and P. Kacman, Phys. Rev. B **67**, 120204(R) (2003).

[24] J. Mašek and F. Máca, Phys. Rev. B **69**, 165212 (2004).

[25] G. Bouzerar, T. Ziman, and J. Kudrnovský, Phys. Rev. B **72**, 125207 (2005).

[26] Y. Takeda, M. Kobayashi, T. Okane, T. Ohkochi, J. Okamoto, Y. Saitoh, K. Kobayashi, H. Yamagami, A. Fujimori, A. Tanaka *et al.*, Phys. Rev. Lett. **100**, 247202 (2008).

[27] M. Zhu, X. Li, G. Xiang, and N. Samarth, Phys. Rev. B **76**, 201201 (2007).

[28] B. Chapler, S. Mack, L. Ju, T. Elson, B. Boudouris, E. Namdas, J. Yuen, A. Heeger, N. Samarth, M. Di Ventra *et al.*, Phys. Rev. B **86**, 165302 (2012).

[29] S. Ohya, K. Takata, and M. Tanaka, Nat. Phys. **7**, 342 (2011).

[30] M. Dobrowolska, K. Tivakornsasithorn, X. Liu, J. K. Furdyna, M. Berciu, K. M. Yu, and W. Walukiewicz, Nat. Mater. **11**, 444 (2012).

[31] W. Dobrowolska, M. Liu, X. Furdyna, J. K. Berciu, M. Yu, and K. M. Walukiewicz, arXiv:1004.4446.

[32] T. Edmonds, K. W. Gallagher, B. L. Wang, M. Rushforth, A. W. Makarovsky, O. Patane, A. Campion, P. Foxon. C. T. Novak and V. Jungwirth, arXiv:1211.3860v1.

[33] D. Basov, R. Averitt, D. van der Marel, M. Dressel, and K. Haule, Rev. Mod. Phys. **83**, 471 (2011).

[34] P. R. Stone, K. Alberi, S. K. Z. Tardif, J. W. Beeman, K. M. Yu, W. Walukiewicz, and O. D. Dubon, Phys. Rev. Lett. **101**, 087203 (2008).

[35] K. Ando, H. Saito, K. C. Agarwal, M. C. Debnath, and V. Zayets, Phys. Rev. Lett. **100**, 067204 (2008).

[36] J.-M. Tang and M. E. Flatté, Phys. Rev. Lett. **101**, 157203 (2008).

[37] J. Mašek, F. Máca, J. Kudrnovský, O. Makarovsky, L. Eaves, R. Campion, K. Edmonds, A. Rushforth, C. Foxon, B. Gallagher *et al.*, Phys. Rev. Lett. **105**, 227202 (2010).

[38] K. Sato and P. H. Dederics, Europhys. Lett. **61**, 403 (2003).

[39] S. Mack, R. C. Myers, J. T. Heron, A. C. Gossard, and D. D. Awschalom, Appl. Phys. Lett. **92**, 192502 (2008).

[40] K. S. Burch, J. Stephens, R. K. Kawakami, D. D. Awschalom, and D. N. Basov, Phys. Rev. B **70**, 205208 (2004).

[41] A. B. Kuzmenko, Rev. Sci. Instrum. **76**, 083108 (2005).

[42] K. Hirakawa, S. Katsumoto, T. Hayashi, Y. Hashimoto, and Y. Iye, Phys. Rev. B **65**, 4 (2002).

[43] K. Hirakawa, Physica E **10**, 215 (2001).

[44] Y. Okimoto, T. Katsufuji, T. Ishikawa, A. Urushibara, T. Arima, and Y. Tokura, Phys. Rev. Lett. **75**, 109 (1995).

[45] K. Alberi, K. M. Yu, P. R. Stone, O. D. Dubon, W. Walukiewicz, T. Wojtowicz, X. Liu, and J. K. Furdyna, Phys. Rev. B **78**, 075201 (2008).

[46] J. Wiley and M. DiDomenico Jr., Phys. Rev. B **2**, 427 (1970).

[47] E. J. Singley, K. S. Burch, R. K. Kawakami, J. Stephens, D. D. Awschalom, and D. N. Basov, Phys. Rev. B **68**, 165204 (2003).

[48] C. P. Moca, G. Zaránd, and M. Berciu, Phys. Rev. B **80**, 165202 (2009).

[49] G. Bouzerar and R. Bouzerar, New J. Phys. **13**, 023002 (2011).

[50] W. Songprakob, R. Zallen, D. V. Tsu, and W. K. Liu, J. Appl. Phys. **91**, 171 (2002).

[51] R. Moriya and H. Munekata, J. Appl. Phys. **93**, 4603 (2003).

[52] T. Jungwirth, J. Sinova, A. H. MacDonald, B. L. Gallagher, V. Novák, K. W. Edmonds, A. W. Rushforth, R. P. Campion, C. T. Foxon, L. Eaves *et al.*, Phys. Rev. B **76**, 125206 (2007).

[53] H. Bebb, Journal of Physics and Chemistry of Solids **28**, 2087 (1967).

[54] H. Bebb, Phys. Rev. **185**, 1116 (1969).

[55] C. A. Huber, J. A. Perez, and T. E. Huber, Phys. Rev. B **36**, 5933 (1987).

[56] E. Kojima, J. B. Héroux, R. Shimano, Y. Hashimoto, S. Katsumoto, Y. Iye, and M. Kuwata-Gonokami, Phys. Rev. B **76**, 195323 (2007).

[57] Y. Nagai and K. Nagasaka, Infrared Phys. Technol. **48**, 1 (2006).

[58] R. Braunstein and E. O. Kane, J. Phys. Chem. Solids **23**, 1423 (1962).

[59] J. Okabayashi, A. Kimura, O. Rader, T. Mizokawa, A. Fujimori, T. Hayashi, and M. Tanaka, Phys. Rev. B **64**, 125304 (2001).

[60] M. A. Mayer, P. R. Stone, N. Miller, H. M. Smith, O. D. Dubon, E. E. Haller, K. M. Yu, W. Walukiewicz, X. Liu, and J. K. Furdyna, Phys. Rev. B **81**, 045205 (2010).

[61] S. Ohya, I. Muneta, P. N. Hai, and M. Tanaka, Phys. Rev. Lett. **104**, 167204 (2010).

[62] T. Dietl and D. Sztenkiel, arXiv:1102.3267v2.

[63] S. Ohya, K. Takata, I. Muneta, P. N. Hai, and M. Tanaka, arXiv:1102.4459.

[64] M. Sawicki, D. Chiba, A. Korbecka, Y. Nishitani, J. A. Majewski, F. Matsukura, T. Dietl, and H. Ohno, Nat. Phys. **6**, 22 (2009).

[65] A. Richardella, P. Roushan, S. Mack, B. Zhou, D. A. Huse, D. D. Awschalom, and A. Yazdani, Science **327**, 665 (2010).